2020
Turkish Journal of
Remote Sensing and GIS

Turkish Journal of Remote Sensing and GIS
Türk Uzaktan Algılama ve CBS Dergisi

Turk J Remote Sens GIS, September 2022, 3(2): 150-159
Journal homepage: http://www.dergipark.org.tr/en/pub/rsgis

Improving the Land Cover Mapping Accuracy of the Sentinel-2 Imagery on Google Earth Engine

Google Earth Engine Üzerinde Sentinel-2 Görüntülerinin Arazi Örtüsü Haritalama Doğruluğunun İyileştirilmesi

Cigdem Serifoglu Yilmaz[1]

[1] *Karadeniz Technical University, Engineering Faculty, Department of Geomatics Engineering, 61080, Trabzon/Turkey.*

ORIGINAL PAPER

***Corresponding author:**
Cigdem Serifoglu Yilmaz
cigdem_srf@hotmail.com

doi: 10.48123/rsgis.1119572

Article history
Received: 21.05.2022
Accepted: 07.08.2022
Published: 18.09.2022

Abstract

Accurate land cover information is necessary for successful monitoring, planning and management of the land cover features. Thanks to free-access satellite images, studies have focused on the creation of more accurate thematic maps, which have been used as a base data in many applications. The cloud-based Google Earth Engine (GEE) service makes it easier to access, store and process these satellite images. This study aims to improve the accuracy of a land cover map produced with the Sentinel-2 satellite image. For this purpose, as the very first step, study site was classified using only traditional bands of the Sentinel-2 data. To improve the classification accuracy, Sentinel-1 Synthetic Aperture Radar (SAR) data, Advanced Land Observing Satellite (ALOS) World 3D data, various spectral indices and gray-level co-occurrence matrix (GLCM) features were added to the traditional bands of the Sentinel-2 data, leading to a multi-source classification process. In this study, where the city center of Trabzon was selected as the study area, the accuracy of the land cover map produced using the Random Forest (RF) classification algorithm was increased from 83.51% to 92.78% with the auxiliary data used.

Keywords: *Google Earth Engine, Land cover mapping, Image classification, Sentinel-2*

Özet

Yeryüzü nesnelerinin başarılı bir şekilde izlenmesi, planlanması ve yönetimi için yüksek doğruluklu arazi örtüsü bilgisi gereklidir. Ücretsiz erişilebilen uydu görüntüleri sayesinde, birçok uygulamada temel altlık verisi olarak kullanılabilen yüksek doğruluklu tematik haritaların oluşturulmasına yönelik çalışmalar yoğunlaşmıştır. Bulut tabanlı Google Earth Engine (GEE) platformu, bu tür uydu görüntülerine erişmeyi, depolamayı ve işlemeyi kolaylaştırmaktadır. Bu çalışma, Sentinel-2 uydu görüntüsü ile üretilmiş bir arazi örtüsü haritasının doğruluğunu artırmayı amaçlamaktadır. Bu amaçla, ilk aşamada, çalışma alanı Sentinel-2 verilerinin yalnızca geleneksel bantları kullanılarak sınıflandırılmıştır. Daha sonra, sınıflandırma doğruluğunu iyileştirmek için Sentinel-2 görüntüsünün geleneksel bantlarına Sentinel-1 Yapay Açıklıklı Radar (SAR) verisi, Gelişmiş Arazi Gözlem Uydusu (ALOS) 3 boyutlu sayısal yükseklik modeli verileri, çeşitli spektral indeksler ve Gri Seviyeli Eşdizimlilik Matrisi (GLCM) özellikleri eklenerek çok kaynaklı bir sınıflandırma prosedürü geliştirilmiştir. Trabzon ilinin şehir merkezinin çalışma bölgesi olarak seçildiği bu çalışmada, Rastgele Orman (RF) sınıflandırma algoritması kullanılarak üretilen arazi örtüsü haritasının doğruluğu kullanılan yardımcı veriler ile %83.51'den %92.78'e yükseltilmiştir.

Anahtar kelimeler: *Google Earth Engine, Arazi örtüsü haritalama, Görüntü sınıflandırma, Sentinel-2*

1. Introduction

With the rapid development in technology, remote sensing methods have become much more important for monitoring the development of land cover and urban areas. The high-resolution information provided by the commercial satellites WorldView, Quickbird and IKONOS enables highly accurate land cover information (Pu, 2011; Akar and Güngör, 2012; Akar et al., 2017; Saralioglu and Gungor, 2020). However, the fact that these satellite images are not free has motivated researchers to use free-of-charge satellite data. The satellites of the Landsat mission (i.e., 4-TM (Thematic Mapper), 5-TM, 7-ETM+ (Enhanced Thematic Mapper Plus), and 8-OLI (Operational Land Imager)), which are in the freely-accessible satellite data category, have been generally used in previous studies for land cover mapping for half a century (Wulder et al., 2019; Nguyen et al., 2021). The Sentinel mission, which is another free-to-use satellite data, has been available since 2015.

The literature reports various studies where different image features were used together with the Sentinel-2 MSI (MultiSpectral Instrument) and Landsat TM/ETM+/OLI images to improve image classification performance (Coulter et al., 2016; Hu et al., 2021). For example, Sentinel-1 SAR data may be used with the Sentinel-2 MSI in situations where the Sentinel-2 MSI has insufficient optical capacity, such as acquiring information from dark surfaces (Hu et al., 2021). Moreover, SAR imagery has been preferred in many studies as an additional feature due to the fact that it is not affected by weather conditions, providing information about the material of the surface structures, and that it is able to penetrate through the soil or vegetation (Weng, 2012; Dong et al., 2020; Chong et al., 2021). Spectral indices that are used to extract valuable information from the imageries are another auxiliary data that can be used to improve the classification performance. The normalized difference vegetation index (NDVI), normalized difference water index (NDWI) and normalized difference built-up index (NDBI) are some of the commonly used spectral indices (Rawat and Kumar, 2015; Ko et al., 2015; Sonobe et al., 2017; Kobayashi et al., 2020). Thanks to their ability to separate different land cover classes and even the land features of similar spectral characteristics with respect to their reflectance at different wavelengths, spectral indices are considered almost indispensable for optical remote sensing observations and practices. The elevation information is also another data source used to increase the image classification performance. Shuttle Radar Topography Mission (SRTM) digital elevation model (DEM) (Shrestha and Saepuloh, 2019; Chen et al., 2021), Advanced Spaceborne Thermal Emission and Reflection Radiometer Global Digital Elevation Model (ASTER GDEM) (Saputra and Lee, 2019; Birhanu et al., 2019), and Advanced Land Observing Satellite (ALOS) World 3D (Maffei Valero et al., 2022) are among the datasets mostly used for improving the classification performance. A significant amount of the previous studies made use of texture extraction filters like gray-level co-occurrence matrix (GLCM) (Haralick et al., 1973) Gabor filter (Xiao et al., 2010; Dumitru et al., 2016) or morphological operators (Iftikhar and Khurshid, 2011). Previous studies showed that textural information can help distinguish class types having different texture but similar spectral features (Ressel et al., 2015; Ayhan and Kwan, 2020).

In this study, the Sentinel-2 MSI data, Sentinel-1 SAR data, ALOS World 3D elevation data, green normalized difference vegetation index (GNDVI) (Gitelson and Merzlyak, 1998), modified normalized difference water index (MNDWI) (Han-Qiu, 2005), normal difference built-up index (NDBI) (Zha et al., 2003), bare soil index (BSI) (Chen et al., 2004), modified bare soil index (MBSI) (Nguyen et al., 2021) and GLCM texture features were employed in different combinations to improve the classification accuracy of the Sentinel-2 optical satellite data. All experiments were conducted in the Google Earth Engine (GEE) (Gorelick et al., 2017) (with JavaScript API code editor), which is a cloud-based Earth observation and analysis platform. The GEE has been resorted a lot in the recent years as it provides a huge amount of open-access geospatial and remote sensing datasets for comfortable and fast processing without any storage space problems (Tsai et al., 2018; Sun et al., 2019; Wagle et al., 2020).

2. Material and Methods

2.1 Study Area

The selected study region, which covers an area of approximately 215 km^2, is in the city centre of Trabzon, which is located in the northeast of Turkey. The coastal parts of the study region are generally urban areas with a dense presence of man-made structures, whereas the inner parts are rural areas. At the same time, the coastal part, which has a relatively flatter topography, turns into a rather rough mountainous terrain as moving inland. The study area is mostly covered by forests and vegetation. Figure 1 shows the study area.

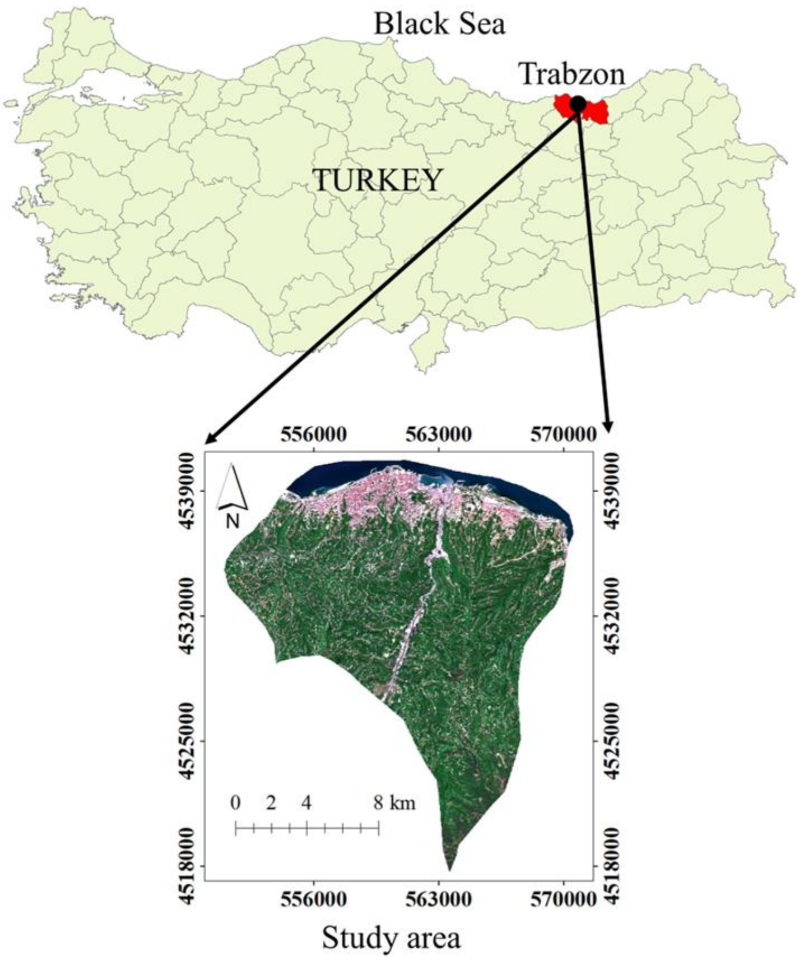

Figure 1. Study area

2.2 Data Used

This study used the Sentinel optical and SAR satellite imageries provided by the European Space Agency (ESA) Copernicus program. The pre-processed Sentinel-2 MSI data (Level 2A, Bottom-Of-Atmosphere (BOA) surface reflectance product) in the GEE collection (collection id: COPERNICUS/S2_SR) was used as the optical imagery. The Sentinel-2 MSI data includes 13 spectral bands with spatial resolutions ranging between 10 m and 60 m (10 m: B2, B3, B4, B8; 20 m: B5, B6, B7, B8A, B11, B12; 60 m: B1, B9, B10; B refers to band) (https://sentinels.copernicus.eu/web/sentinel/user-guides/sentinel-2-msi/resolutions/spatial). The image collections were filtered with cloudy pixel percentage less than 5% to ensure working with clear image. Of the 21 images in the image collection created for May 2021, three images remained after cloud filtering. To provide balance among the pixel values of the image, median reducer function was applied and the image to be classified was generated. The SAR data was also acquired through the GEE with collection id: 'COPERNICUS/S1_GRD'. The pre-processed collection offers Sentinel-1 (C-band) Ground Range Detected (GRD) scenes with orbit file correction, GRD border noise removal, thermal noise removal, radiometric calibration, and terrain correction applied using the SRTM 30 m or ASTER DEM (https://developers.google.com/earth-engine/guides/sentinel1). The 10-m Sentinel-1 images were acquired in the Interferometric Wide Swath (IW) mode with two polarizations as vertical transmit/vertical receive (VV) and vertical transmit/horizontal receive (VH), with descending mode. A refined Lee filter with a pixel size of 9 × 9 was then used to remove the speckle noise of the SAR data (Lee et al., 2008). Plenty of attention was paid in this study to select the optical and SAR images with close acquisition dates. The SAR data was acquired on the 16th of May, 2021, whereas the optical data was generated as the median of the imageries acquired on the 12th, 15th and 20th of May 2021. The ALOS World 3D – 30 meter (AW3D30) DEM data was used to introduce the elevation and slope information to the classifier. This study used the updated version (ver 3.2) of the AW3D30, which is available in the GEE platform with collection id: 'JAXA/ALOS/AW3D30/V3_2' (Tadono et al., 2014; Takaku et al., 2014; Takaku et al., 2016; Tadono et al., 2016).

2.3 Methodology

Different scenarios were designed to improve the accuracy of the land cover maps produced with the Sentinel-2 satellite image. The first scenario considers only the traditional bands (B2, B3, B4, B8) of the Sentinel-2 image for classification. All spectral bands of the Sentinel-2 data except the B1 (coastal aerosol band) and B10 (SWIR-cirrus band) were classified in the second scenario. The spectral indices GNDVI, MNDWI, NDBI, BSI and MBSI, which were calculated through the Sentinel-2 bands, were included in the classification in the third scenario. The fourth scenario includes the elevation and slope data obtained from the AW3D30 in the classification. The fifth scenario incorporates the VV and VH polarizations of the Sentinel-1 SAR data. In the last scenario, the four GLCM metrics, namely angular second moment (asm), contrast (contrast), difference variance (dvar) and information measure of correlation 2 (imcorr2), were computed from the first principal component of the Sentinel-2 data transformed into the PCA (principal component analysis) domain. The GEE offers 14 GLCM features (Haralick et al., 1973) and four additional textural features (Conners et al., 1984). Four texture features used in this study were selected after various trials.

Table 1. The spectral indices used in this study

Indices Used	Abbreviation	Formulation
Green Normalized Difference Vegetation Index	GNDVI	(NIR - Green) / NIR + Green)
Modified Normalized Difference Water Index	MNDWI	(Green - SWIR1) / Green + SWIR1)
Normal Difference Built-up Index	NDBI	(SWIR1 - NIR) / SWIR1 + NIR)
Bare Soil Index	BSI	((SWIR1 + Red) - (NIR + Blue)) / ((SWIR1 + Red) + (NIR + Blue))
Modified Bare Soil Index	MBSI	((SWIR1 - SWIR2 - NIR) / (SWIR1 + SWIR2 + NIR)) + 0.5

In the first phase of the implementation, pixel samples were collected for five classes, including built-up, water, bare-soil, forest and vegetation. Table 2 presents further details on the classes. The number of the test points required to evaluate the classification result was estimated with respect to the multinomial distribution approach (Congalton and Green, 2019; Yilmaz et al., 2018; Yilmaz, 2021). This approach revealed that a minimum of 663 validation points had to be used for a reasonable accuracy assessment. To increase the robustness of the accuracy assessment, the number of the validation points used was set to a much greater value than needed. Hence, a total of 5727 pixel samples were collected for all land classes. The collected pixel samples were then divided into two groups, approximately 70% (i.e., 3996 pixels) of them for training and 30% (i.e., 1731 pixels) of them for validation. The validation data included 438, 83, 272, 556 and 382 pixels for the built-up, water, bare-soil, forest and vegetation classes, respectively. Since the water class had a homogeneous colour content, relatively smaller number of pixels were collected for this class. Afterwards, a non-parametric machine learning algorithm, the random forest (RF), was used to classify the images produced within each scenario. The RF was preferred due to its flexibility, robust performance and easy-to-tune hyper-parameters (Rodriguez-Galiano, 2012; Akar and Güngör, 2012). (1) Number of trees (ntree - “numberOfTrees”), (2) number of variables to split the nodes of trees (mtry - “variablesPerSplit”), (3) minimum leaf population (“minLeafPopulation”), (4) fraction of input to bag per tree (“bagFraction”), (5) maximum number of leaf nodes (“maxNodes”), and (6) random seed variable (“seed”) are six input parameters required to tune the algorithm. Since the ntree and mtry are the most critical parameters of the RF (Amani et al., 2017), extreme care was taken while specifying their values. As a result of the trials, setting the ntree parameter to 60 and the mtry parameter to the number of input features (bands) in each scenario was found to have led to the best RF performance. The remaining four parameters were set to their default input values (https://developers.google.com/earth-engine/apidocs/ee-classifier-smilerandomforest).

Table 2. Description for the land cover classes considered in the study

Land Classes	Class Description
Built-up	All settlements, industrial areas, roads, coastal structures including harbor, pier, breakwater
Water	All water bodies including sea, river
Bare-soil	Soil or sand that is not cover by grass or other plants
Forest	Mixed tree varieties
Vegetation	All cultivated and uncultivated plants

The accuracy of the classified images was evaluated thorough the validation data consisting of 1731 pixel samples. The accuracy of each land cover map produced within each scenario was evaluated through the confusion matrix derived based on the comparison of the classification outputs with the ground truth samples (Congalton, 1991; Tassi et al., 2021). The confusion matrices produced include the producer's accuracy (PA), user's accuracy (UA) and overall accuracy (OA) (Congalton and Green, 2019) metrics. The PA indicates the probability of a reference pixel being correctly classified, whereas the UA indicates the probability that a classified pixel is actually from that class on the ground. The OA, as its name implies, shows the general classification accuracy and is computed by dividing the total number of correctly classified pixels to the total number of reference pixels (Congalton, 1991; Liu et al., 2007).

3. Results and Discussion

This section investigates to what extent each scenario affected the OA, PA and UA. Figures 2 and 3 present the land cover maps produced for all scenarios. The accuracy of the land cover maps produced within all scenarios were investigated quantitatively.

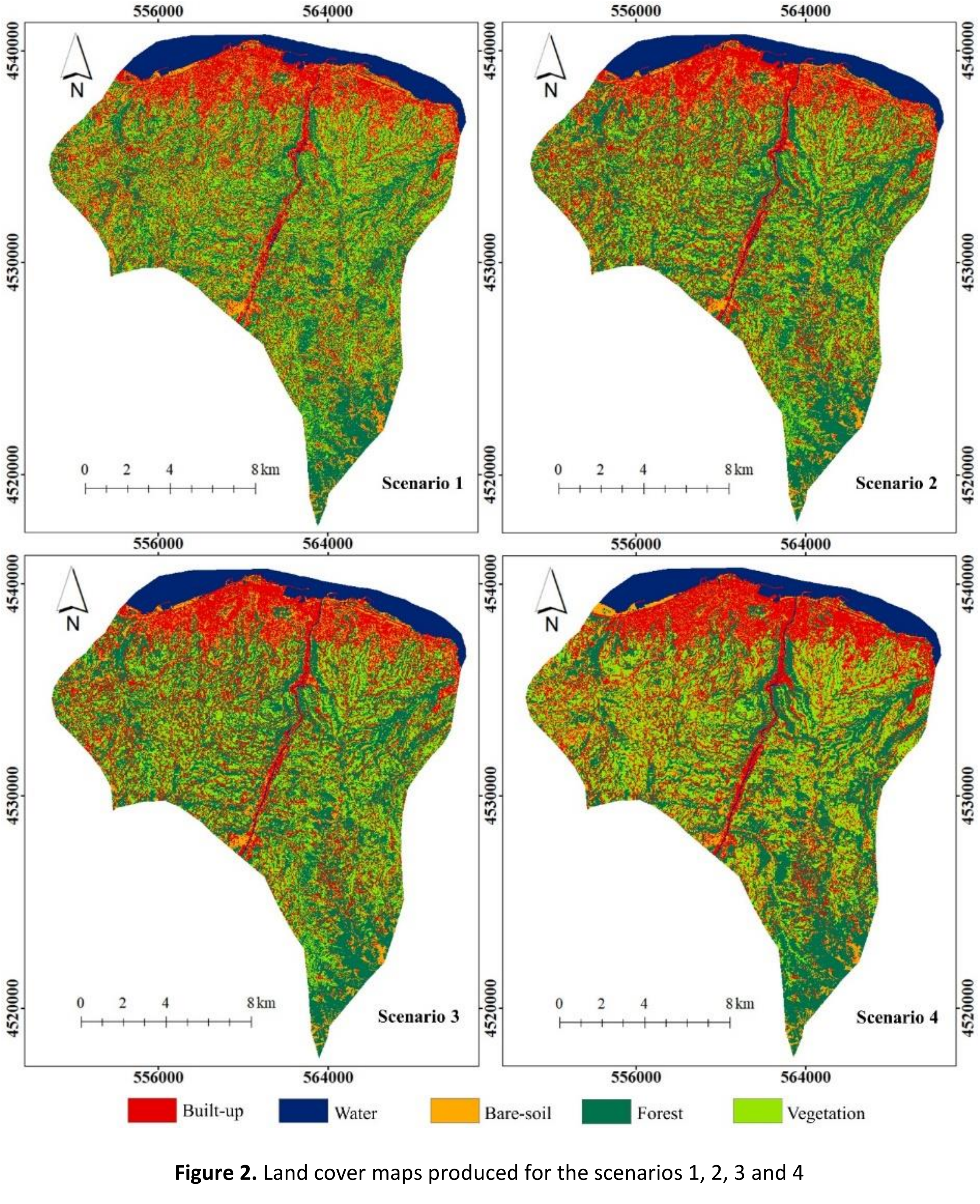

Figure 2. Land cover maps produced for the scenarios 1, 2, 3 and 4

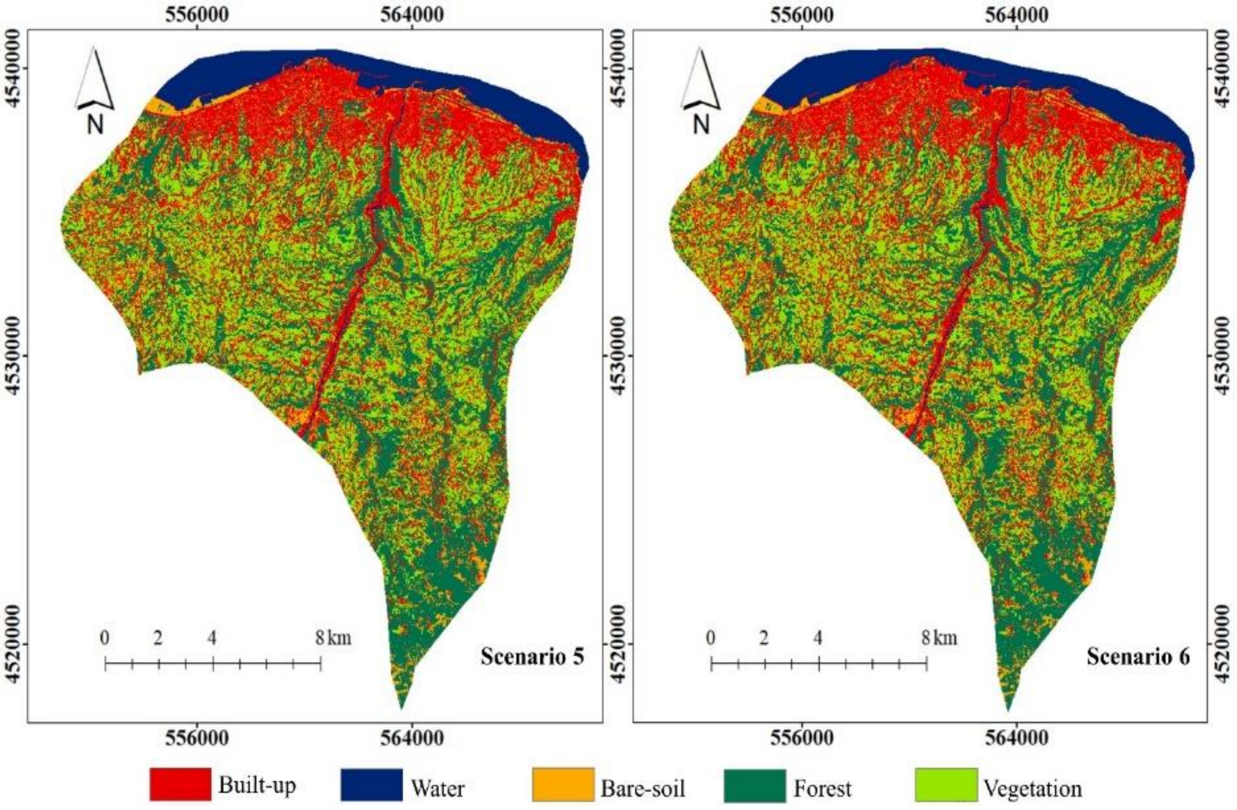

Figure 3. Land cover maps produced for the scenarios 5 and 6

The PA, UA, F-1 score (Ustuner and Balik Sanli, 2019; Tonbul et al., 2022) and OA values derived from the classified maps are given in Table 3. As seen in the table, in the first scenario, the traditional bands of the Sentinel-2 data resulted in the best PA and UA for the water class, which shows that the reference water pixels are classified with a high accuracy and that the classes other than water were generally not misclassified as water. The lowest PA (73.37%) and UA (76.19%) for this scenario were obtained for the vegetation and bare-soil classes, respectively. The lowest and highest F-1 scores were obtained by the vegetation and water classes in this scenario, respectively. The OA achieved for this scenario was found to be 83.51%. Table 3 shows that, in the second scenario, the greatest PA was achieved for the water class and the greatest UA was obtained for the vegetation class. The lowest PA and UA were obtained for the bare-soil class in this scenario. The lowest and highest F-1 scores were obtained by the bare-soil and forest classes in this scenario, respectively. The OA for this scenario was calculated as 85.70%.

As can be seen, using 11 bands of the Sentinel-2 data slightly increased the OA. In the third scenario, the greatest PA and UA were achieved for the water and forest classes, correspondingly. On the other hand, the bare-soil class was found to be the one that was found with the lowest accuracy, which was also the case in the second scenario. The bare-soil and forest classes received the lowest and highest F-1 scores in this scenario, correspondingly. The OA of the third scenario was computed as 86.27%. This reveals the fact that adding the spectral indices to the dataset of the second scenario led to a slight increase in the OA. It can also be concluded that, in this scenario, adding the spectral indices into the classification procedure resulted in a considerable increase in the classification accuracy of the forest and vegetation classes. As seen in Table 3, the highest PA was achieved for the water class in the fourth scenario. The table also shows that the lowest UA was obtained for the bare-soil class. The bare-soil and water classes led to the lowest and highest F-1 scores in this scenario, correspondingly. This scenario has an interesting point. As seen in the table, 82.72% of the reference bare-soil pixels were correctly classified, which can be considered a relatively good classification accuracy. However, 66.77% of the pixels classified as bare-soil were actually bare-soil pixels. In other words, a user who has an intention to use this land cover map on the field will notice that 33.23% of the pixels were misclassified with respect to the current condition of the field. Table 3 also depicts that, in the fifth scenario, the greatest PA and UA were achieved for the water and forest class, respectively. On the other hand, the lowest PA and UA were obtained for the built-up and bare-soil classes, respectively. The lowest and highest F-1 scores were obtained by the bare-soil and water classes in this scenario, respectively. The OA achieved for this scenario was calculated as 89.02%. As can be seen, including the VV and VH polarizations of the Sentinel-1 SAR data into the classification made a considerable contribution to the OA.

In the sixth scenario, the class that was best separated from the others was the forest class as a PA and UA of 97.84% and 98.73% were achieved for this class as a result of the classification. The lowest PA and UA were obtained for the bare-soil class. The bare-soil and forest classes led to the lowest and highest F-1 scores in this scenario, correspondingly. The OA of the sixth scenario was found to be 92.78%. As can be seen, adding the Sentinel-2 bands B5, B6, B7, B8A, B9, B11 and B12; spectral indices; topographic features; SAR information and GLCM features to the traditional Sentinel-2 MSI bands led to an 11.10% increase in the OA.

Table 3. PA, UA, F-1 score and OA metric values computed for all scenarios

Scenario		Class	PA (%)	UA (%)	F-1 score (%)	OA (%)
1	• Sentinel-2 MSI (B2, B3, B4, B8)	**Built-up**	84.02	91.77	87.72	**83.51**
		Water	92.77	90.59	91.67	
		Bare-soil	82.35	76.19	79.15	
		Forest	89.20	81.95	85.42	
		Vegetation	73.37	81.21	77.09	
2	• Sentinel-2 MSI (all bands except B1 and B10)	**Built-up**	85.16	86.95	86.05	**85.70**
		Water	97.59	79.41	87.57	
		Bare-soil	73.90	78.52	76.14	
		Forest	92.74	87.33	89.95	
		Vegetation	81.72	88.42	84.94	
3	• Sentinel-2 MSI (all bands except B1 and B10) • GNDVI, MNDWI, NDBI, BSI, MBSI	**Built-up**	85.39	87.38	86.37	**86.27**
		Water	97.59	81.82	89.01	
		Bare-soil	73.90	78.21	75.99	
		Forest	92.39	88.62	90.47	
		Vegetation	84.60	88.04	86.29	
4	• Sentinel-2 MSI (all bands except B1 and B10) • GNDVI, MNDWI, NDBI, BSI, MBSI • AW3D30 - DEM and slope	**Built-up**	77.17	89.89	83.05	**88.28**
		Water	97.59	97.59	97.59	
		Bare-soil	82.72	66.77	73.89	
		Forest	96.81	95.12	95.96	
		Vegetation	90.34	93.80	92.04	
5	• Sentinel-2 MSI (all bands except B1 and B10) • GNDVI, MNDWI, NDBI, BSI, MBSI • AW3D30 - DEM and slope • Sentinel-1 SAR - VV and VH	**Built-up**	78.99	90.34	84.28	**89.02**
		Water	97.59	96.43	97.01	
		Bare-soil	83.82	68.06	75.12	
		Forest	96.76	96.59	96.67	
		Vegetation	91.10	93.55	92.31	
6	• Sentinel-2 MSI (all bands except B1 and B10) • GNDVI, MNDWI, NDBI, BSI, MBSI • AW3D30 - DEM and slope • Sentinel-1 SAR - VV and VH • GLCM features	**Built-up**	90.18	90.39	90.28	**92.78**
		Water	97.59	96.43	97.01	
		Bare-soil	82.35	80.00	81.16	
		Forest	97.84	98.73	98.28	
		Vegetation	94.76	95.51	95.13	

The water class was successfully separated from the other classes in all scenarios, which is not surprising as the spectral features of the pixels of this class were much different than the pixels of the other classes. The forest and vegetation classes have spectrally similar features, which, of course, makes it more challenging to separate them, especially with a spatial resolution of 10 m. As can be seen in Table 3, including the DEM and slope information; VV and VH polarizations of the Sentinel-1 SAR data; and GLCM features into the classification procedure, played a significant role in the discrimination of these classes. The GLCM features were also found to have made a considerable contribution to the OA as they increased the OA achieved in the fifth scenario by 4.22%.

4. Conclusion

This study aimed to increase the RF classification performance of the Sentinel-2 data with the aid of auxiliary data such as spectral indices, topographical features, SAR information and GLCM texture features. These features were used to form different scenarios in the GEE platform and to what degree each scenario affected the OA was investigated. All of the auxiliary data used was found to increase the overall classification accuracy to a certain degree. However, the greatest OA increase was achieved as a result of the inclusion of the GLCM features into the classification procedure.

Although the SAR data was expected to make a good contribution to the classification accuracy, the experiments revealed the opposite. Despite the Lee filtering, SAR data still included a certain amount of noise, which is why it did not make a considerable contribution to the classification accuracy. It was also concluded that the ntree and mtry parameters of the RF classifier had a significant effect on the classification performance. The GEE makes it easier to observe and manage large-extent areas, which is a huge advantage compared to traditional techniques. On the other hand, the GEE includes hundreds of easy-to-use built-in functions in both Python and JavaScript environments, which makes it efficient for analysts. It offers widely-used satellite imageries such as MODIS, Landsat, Sentinel etc., together with their achieve imageries. Its rich data content and easy-to-use data analysis capabilities make the GEE one of the best cloud computing platforms for remote sensing applications.

References

Akar, A., Gökalp, E., Akar, Ö., & Yılmaz, V. (2017). Improving classification accuracy of spectrally similar land covers in the rangeland and plateau areas with a combination of WorldView-2 and UAV images. *Geocarto International*, *32*(9), 990-1003.

Akar, Ö., & Güngör, O. (2012). Classification of multispectral images using Random Forest algorithm. *Journal of Geodesy and Geoinformation*, *1*(2), 105-112.

Amani, M., Salehi, B., Mahdavi, S., Granger, J. E., Brisco, B., & Hanson, A. (2017). Wetland classification using multi-source and multi-temporal optical remote sensing data in Newfoundland and Labrador, Canada. *Canadian Journal of Remote Sensing*, *43*(4), 360-373.

Ayhan, B., & Kwan, C. (2020). Tree, shrub, and grass classification using only RGB images. *Remote Sensing*, *12*(8), 1333. doi: 10.3390/rs12081333.

Birhanu, L., Hailu, B. T., Bekele, T., & Demissew, S. (2019). Land use/land cover change along elevation and slope gradient in highlands of Ethiopia. *Remote Sensing Applications: Society and Environment*, *16*, 100260. doi: 10.1016/j.rsase.2019.100260.

Chen, D., Shevade, V., Baer, A., He, J., Hoffman-Hall, A., Ying, Q., ... & Loboda, T. V. (2021). A disease control-oriented land cover land use map for Myanmar. *Data*, *6*(6), 63-78.

Chen, W., Liu, L., Zhang, C., Wang, J., Wang, J., & Pan, Y. (2004, September). Monitoring the seasonal bare soil areas in Beijing using multitemporal TM images. In *IGARSS 2004 - 2004 IEEE International Geoscience and Remote Sensing Symposium* (Vol. 5, pp. 3379-3382). IEEE.

Chong, L. U. O., Liu, H. J., Lu, L. P., Liu, Z. R., Kong, F. C., & Zhang, X. L. (2021). Monthly composites from Sentinel-1 and Sentinel-2 images for regional major crop mapping with Google Earth Engine. *Journal of Integrative Agriculture*, *20*(7), 1944-1957.

Congalton, R. G. (1991). A review of assessing the accuracy of classifications of remotely sensed data. *Remote sensing of environment*, *37*(1), 35-46.

Congalton, R. G., & Green, K. (2019). *Assessing the accuracy of remotely sensed data: principles and practices*. Boca Raton, FL: CRC press.

Conners, R. W., Trivedi, M. M., & Harlow, C. A. (1984). Segmentation of a high-resolution urban scene using texture operators. *Computer Vision, Graphics, and Image Processing*, *25*(3), 273-310.

Coulter, L. L., Stow, D. A., Tsai, Y. H., Ibanez, N., Shih, H. C., Kerr, A., ... & Mensah, F. (2016). Classification and assessment of land cover and land use change in southern Ghana using dense stacks of Landsat 7 ETM+ imagery. *Remote Sensing of Environment*, *184*, 396-409.

Dong, D., Wang, C., Yan, J., He, Q., Zeng, J., & Wei, Z. (2020). Combing Sentinel-1 and Sentinel-2 image time series for invasive Spartina alterniflora mapping on Google Earth Engine: a case study in Zhangjiang Estuary. *Journal of Applied Remote Sensing*, *14*(4), 044504. doi: 10.1117/1.JRS.14.044504.

Dumitru, C. O., Schwarz, G., Cui, S., & Datcu, M. (2016, May). Improved image classification by proper patch size selection: TerraSAR-X vs. sentinel-1A. In *2016 International Conference on Systems, Signals and Image Processing (IWSSIP), 2016. Proceedings.* (pp. 1-4). IEEE.

Gitelson, A. A., & Merzlyak, M. N. (1998). Remote sensing of chlorophyll concentration in higher plant leaves. *Advances in Space Research*, *22*(5), 689-692.

Gorelick, N., Hancher, M., Dixon, M., Ilyushchenko, S., Thau, D., & Moore, R. (2017). Google Earth Engine: Planetary-scale geospatial analysis for everyone. *Remote Sensing of Environment*, *202*, 18-27.

Han-Qiu, X. U. (2005). A study on information extraction of water body with the modified normalized difference water index (MNDWI). *Journal of Remote Sensing*, *9*(5), 589-595.

Haralick, R. M., Shanmugam, K., & Dinstein, I. H. (1973). Textural features for image classification. *IEEE Transactions on Systems, Man, and Cybernetics*, *SMC-3*(6), 610-621.

Hu, B., Xu, Y., Huang, X., Cheng, Q., Ding, Q., Bai, L., & Li, Y. (2021). Improving Urban Land Cover Classification with Combined Use of Sentinel-2 and Sentinel-1 Imagery. *ISPRS International Journal of Geo-Information*, *10*(8), 533-549.

Iftikhar, H., & Khurshid, K. (2011, November). Fusion of gabor filter and morphological operators for the detection of settlement zones in google earth satellite images. In *2011 IEEE International Conference on Signal and Image Processing Applications (ICSIPA). Proceedings.* (pp. 232-237). IEEE.

Ko, B. C., Kim, H. H., & Nam, J. Y. (2015). Classification of potential water bodies using Landsat 8 OLI and a combination of two boosted random forest classifiers. *Sensors*, *15*(6), 13763-13777.

Kobayashi, N., Tani, H., Wang, X., & Sonobe, R. (2020). Crop classification using spectral indices derived from Sentinel-2A imagery. *Journal of Information and Telecommunication*, *4*(1), 67-90.

Lee, J. S., Wen, J. H., Ainsworth, T. L., Chen, K. S., & Chen, A. J. (2008). Improved sigma filter for speckle filtering of SAR imagery. *IEEE Transactions on Geoscience and Remote Sensing, 47*, 202–213.

Liu, C., Frazier, P., & Kumar, L. (2007). Comparative assessment of the measures of thematic classification accuracy. *Remote Sensing of Environment*, *107*(4), 606-616.

Maffei Valero, M. A., Araújo, W. F., Melo, V. F., Augusti, M. L., & Fernandes Filho, E. I. (2022). Land-use and land-cover mapping using a combination of radar and optical sensors in Roraima–Brazil. *Engenharia Agrícola*, *42*(2), e20210142. doi: 10.1590/1809-4430-Eng.Agric.v42n2e20210142/2022.

Nguyen, C. T., Chidthaisong, A., Kieu Diem, P., & Huo, L. Z. (2021). A modified bare soil index to identify bare land features during agricultural fallow-period in southeast Asia using Landsat 8. *Land*, *10*(3), 231-248.

Pu, R., Landry, S., & Yu, Q. (2011). Object-based urban detailed land cover classification with high spatial resolution IKONOS imagery. *International Journal of Remote Sensing*, *32*(12), 3285-3308.

Rawat, J. S., & Kumar, M. (2015). Monitoring land use/cover change using remote sensing and GIS techniques: A case study of Hawalbagh block, district Almora, Uttarakhand, India. *The Egyptian Journal of Remote Sensing and Space Science*, *18*(1), 77-84.

Ressel, R., Frost, A., & Lehner, S. (2015). A neural network-based classification for sea ice types on X-band SAR images. *IEEE Journal of Selected Topics in Applied Earth Observations and Remote Sensing*, *8*(7), 3672-3680.

Rodriguez-Galiano, V. F., Chica-Olmo, M., Abarca-Hernandez, F., Atkinson, P. M., & Jeganathan, C. (2012). Random Forest classification of Mediterranean land cover using multi-seasonal imagery and multi-seasonal texture. *Remote Sensing of Environment*, *121*, 93-107.

Saputra, M. H., & Lee, H. S. (2019). Prediction of land use and land cover changes for north sumatra, Indonesia, using an artificial-neural-network-based cellular automaton. *Sustainability*, *11*(11), 3024-3040.

Saralioglu, E., & Gungor, O. (2020). Semantic segmentation of land cover from high resolution multispectral satellite images by spectral-spatial convolutional neural network. *Geocarto International*, 37(2), 657-677.

Shrestha, D. P., Saepuloh, A., & van der Meer, F. (2019). Land cover classification in the tropics, solving the problem of cloud covered areas using topographic parameters. *International Journal of Applied Earth Observation and Geoinformation*, *77*, 84-93.

Sonobe, R., Yamaya, Y., Tani, H., Wang, X., Kobayashi, N., & Mochizuki, K. I. (2017). Mapping crop cover using multi-temporal Landsat 8 OLI imagery. *International Journal of Remote Sensing*, *38*(15), 4348-4361.

Sun, Z., Xu, R., Du, W., Wang, L., & Lu, D. (2019). High-resolution urban land mapping in China from sentinel 1A/2 imagery based on Google Earth Engine. *Remote Sensing*, *11*(7), 752. doi: 10.3390/rs11070752.

Tadono, T., Ishida, H., Oda, F., Naito, S., Minakawa, K., & Iwamoto, H. (2014). Precise global DEM generation by ALOS PRISM. *ISPRS Annals of the Photogrammetry, Remote Sensing and Spatial Information Sciences*, *2*(4), 71-76.

Tadono, T., Nagai, H., Ishida, H., Oda, F., Naito, S., Minakawa, K., & Iwamoto, H. (2016). Generation of the 30 M-mesh global digital surface model by ALOS PRISM. *International Archives of the Photogrammetry, Remote Sensing & Spatial Information Sciences*, XLI-B4(*41), 157-162*.

Takaku, J., Tadono, T., & Tsutsui, K. (2014). Generation of High Resolution Global DSM from Alos Prism. *ISPRS Annals of Photogrammetry, Remote Sensing & Spatial Information Sciences*, XL(4), 243-248.

Takaku, J., Tadono, T., Tsutsui, K., & Ichikawa, M. (2016). Validation of 'AW3D' Global DSM Generated from Alos Prism. *ISPRS Annals of Photogrammetry, Remote Sensing & Spatial Information Sciences*, *III*(4), 25-31.

Tassi, A., Gigante, D., Modica, G., Di Martino, L., & Vizzari, M. (2021). Pixel-vs. Object-based landsat 8 data classification in google earth engine using random forest: The case study of maiella national park. *Remote Sensing*, *13*(12), 2299.

Tonbul, H., Colkesen, I., & Kavzoglu, T. (2022). Pixel-and Object-Based ensemble learning for forest burn severity using USGS FIREMON and Mediterranean condition dNBRs in Aegean ecosystem (Turkey). *Advances in Space Research*, *69*(10), 3609-3632.

Tsai, Y. H., Stow, D., Chen, H. L., Lewison, R., An, L., & Shi, L. (2018). Mapping vegetation and land use types in Fanjingshan National Nature Reserve using google earth engine. *Remote Sensing*, *10*(6), 927-941.

Ustuner, M., & Balik Sanli, F. (2019). Polarimetric target decompositions and light gradient boosting machine for crop classification: A comparative evaluation. *ISPRS International Journal of Geo-Information*, *8*(2), 97-112.

Wagle, N., Acharya, T. D., Kolluru, V., Huang, H., & Lee, D. H. (2020). Multi-temporal land cover change mapping using google earth engine and ensemble learning methods. *Applied Sciences*, *10*(22), 8083-8103.

Weng, Q. (2012). Remote sensing of impervious surfaces in the urban areas: Requirements, methods, and trends. *Remote Sensing of Environment*, *117*, 34-49.

Wulder, M. A., Loveland, T. R., Roy, D. P., Crawford, C. J., Masek, J. G., Woodcock, C. E., ... & Zhu, Z. (2019). Current status of Landsat program, science, and applications. *Remote Sensing of Environment*, *225*, 127-147.

Xiao, P., Feng, X., An, R., & Zhao, S. (2010). Segmentation of multispectral high-resolution satellite imagery using log Gabor filters. *International Journal of Remote Sensing*, *31*(6), 1427-1439.

Yilmaz, V. (2021). Investigation of the performances of advanced image classification-based ground filtering approaches for digital terrain model generation. *Concurrency and Computation: Practice and Experience*, *33*(13), e6219. doi: 10.1002/cpe.6219.

Yilmaz, V., Konakoglu, B., Serifoglu, C., Gungor, O., & Gökalp, E. (2018). Image classification-based ground filtering of point clouds extracted from UAV-based aerial photos. *Geocarto International*, *33*(3), 310-320.

Zha, Y., Gao, J., & Ni, S. (2003). Use of normalized difference built-up index in automatically mapping urban areas from TM imagery. *International Journal of Remote Sensing, 24*(3), 583-594.